Short wavelength infra-red (SWIR) characteristics of hydrothermal alteration minerals in skarn deposits: Example from the Jiguanzui Cu–Au deposit, Eastern China

Jing Tian[a,b], Yu Zhang[c,*], Jia-min Cheng[a,b], Si-quan Sun[d], Yi-jun Zhao[d]

[a] Key Laboratory of Mineralogy and Metallogeny, Guangzhou Institute of Geochemistry, Chinese Academy of Sciences, Guangzhou 510640, China
[b] Graduate University of Chinese Academy of Sciences, Beijing 100049, China
[c] School of Geosciences and Info-Physics, Central South University, South Lushan Road, Changsha 410083, China
[d] Geological Survey of Hubei Province, Wuhan 430034, Hubei, China

ARTICLE INFO

ABSTRACT

The Jiguanzui Cu–Au deposit is an important skarn deposit in the Edong ore district of the Middle–Lower Yangtze River Valley metallogenic belt (MLYRB, Eastern China). The mineralization occurred dominantly in the Lower-Middle Triassic Jialingjiang Formation marble, either along interlayer fracture zones or along the intrusive contact with the Early Cretaceous quartz diorite. Based on the mineral assemblages and textural relationships, the Jiguanzui alteration/mineralization can be divided into five stages, namely (I) prograde skarn alteration (garnet-pyroxene), (II) retrograde alteration (hornblende-epidote-actinolite), (III) hematite mineralization, (IV) quartz-sericite-pyrite-chalcopyrite mineralization (main Cu-Au mineralization stage) and (V) calcite-sulfide mineralization (pyrite-chalcopyrite-molybdenite-galena-sphalerite).

Systematic short wavelength infrared (SWIR) spectral analyses show that alteration minerals at Jiguanzui include mainly sericite group minerals (montmorillonite, illite and muscovite), kaolinite, and carbonate minerals (calcite, ankerite and dolomite), with minor chlorite, halloysite and dickite. Spectral features of Stage IV sericite group minerals indicate that the Al-OH absorption feature wavelength positions (Pos2200) have shifted toward longer wavelengths (> 2209 nm) in the ore proximal area, which may be caused by the substitution of Fe and Mg in the octahedral Al site. The vertical distance of mineralization indication can reach up to ca. 450 m, but can be affected by the wall-rock lithology and the Jiguanshan fault zone. The Fe-OH absorption feature wavelength positions (Pos2250) of chlorite in the Middle Triassic Puqi Formation hornfels have also shifted toward longer wavelengths in the ore proximal area, which may be caused by the relative Mg-rich nature of the chlorite. We conclude that the high Pos2200 (> 2209 nm) of sericite group minerals and the high Pos2250 of chlorite can be used as prospecting tools for the Jiguanzui Cu–Au skarn mineralization.

1. Introduction

Short wavelength infrared (SWIR) spectra (wavelength = 1300–2500 nm) are between the near-infrared and mid-infrared light electromagnetic waves. Based on reflectance and absorption, molecular bonds of H_2O, OH, CO_3, NH_4, Al-OH, Fe-OH and Mg-OH can be identified in this spectral range (Thompson et al., 1999; Yang et al., 2012), which can be used to determine a wide range of mineral groups, including phyllosilicates, hydroxylated silicates and sulfates, carbonates, and ammonium-bearing minerals (Pontual et al., 1997). For some minerals (e.g., sericite group minerals and chlorite), the relationship between the spectral absorption wavelengths and the mineral

compositional variations can be used to estimate the compositions of these minerals (Herrmann et al., 2001), leading to the development of field-based SWIR technology for rapid alteration mineral identification and alteration zone delineation (Herrmann et al., 2001). More importantly, SWIR spectral analyses have also been used as vectoring tools to locate the hydrothermal centers (Thompson et al., 1999; Herrmann et al., 2001; Harraden et al., 2013; Tappert et al., 2013; Laakso et al., 2016), with some degree of success (Table 1), e.g., porphyry Cu deposits such as Tuwu in Xinjiang (China) (Yang et al., 2005), Xinan in Fujian (China) (Xu et al., 2017), and Pebble in Alaska (US) (Harraden et al., 2013), and volcanogenic massive sulfide (VMS) deposits such as Rosebery in Tasmania (Australia) (Herrmann et al., 2001), Myra Falls in

---

* Corresponding author.
  E-mail address: zyu2005@csu.edu.cn (Y. Zhang).

Table 1
Summary of the spectral parameter for some porphyry, VMS and very few skarn deposits in the world.

Deposit	Spectral parameter	Proximal mineralization	Distal mineralization	Reference
Tuwu porphyry Cu deposit	AlOH wavelength (nm)	2190–2206	2196–2218	Yang et al. (2005)
	FeOH wavelength (nm)	long	short	
Pebble porphyry Cu–Au–Mo deposit	AlOH wavelength (nm)	2190–2210	2210–2220	Harraden et al. (2013)
Xinan porphyry Cu–Mo deposit	AlOH wavelength (nm)	> 2203	< 2203	Xu et al. (2017)
	Illite crystallinity	> 2.1	< 2.1	
Rosebery VMS deposit	AlOH wavelength (nm)	2190–2200	> 2200	Herrmann et al. (2001)
Myra Falls VMS deposit	AlOH wavelength (nm)	2194–2204	2194–2218	Jones et al. (2005)
	FeOH wavelength (nm)	2238–2252	2238–2255	
Izok Lake VMS deposit	AlOH wavelength (nm)	Short; intermediate zone: long	Short	Laakso et al. (2016)
	FeOH wavelength (nm)	Short; intermediate zone: long	Short	
Honghai VMS deposit	AlOH wavelength (nm)	short	long	Huang et al. (2018)
Tonglvshan skarn deposit	FeOH wavelength (nm)	> 2253	< 2253	Zhang et al. (2017)

British Columbia (Canada) (Jones et al., 2005), Izok Lake in Nunavut (Canada) (Laakso et al., 2016) and Honghai in Xinjiang (China) (Huang et al., 2018). However, reports on successful SWIR applications on skarn deposit prospecting are fairly limited (Zhang et al., 2017a).

The Jiguanzui Cu–Au skarn deposit, with a proven ore reserve of 5.6 Mt at 4.87 g/t Au and 181 Mt at 1.03% Cu (Qiu, 1995; Zhao et al., 1999; Pan and Dong, 1999), is an important skarn deposit in the Edong ore district of the Middle–Lower Yangtze River Valley metallogenic belt (MLYRB), Eastern China. Previous research on the Jiguanzui Cu–Au deposit has mainly focused on: 1) age of the ore-causative intrusions and magmatic evolution (Li et al., 2009a; Mao et al., 2011; Duan et al., 2017); 2) ore deposit geology, including the geophysical and geochemical features (Zhang, 1994; Qiu, 1995; Liu et al., 1996; Pan, 2004; Wei et al., 2006; Guo et al., 2007; Ke et al., 2016); 3) ore-forming mechanism (Xiao et al., 2003; Zhang et al., 2005a, 2011; Wei et al., 2013; Xiao et al., 2003; Zhang, 2015; Zhang et al., 2016). However, the detailed study of alteration zonation and altered minerals is inadequate at Jiguanzui, in particular, little attention has been paid on their indication to the mineralization (or hydrothermal center). Such study combined with a new method, e.g., SWIR analysis, may provide new insights for our understanding of alteration-mineralization process and also bring new criteria for future exploration at Jiguanzui ore district.

In this study, we conducted systematic SWIR spectral analyses on the alteration minerals from Jiguanzui to determine the mineral contents and features, based on fine mineralization paragenetic classification. We discussed the correlation between the skarn mineralization and the SWIR absorption feature of ore-related alteration minerals at Jiguanzui. This correlation may provide help for the mineral prospecting at Jiguanzui, and it may also be important for guiding to the exploration of similar skarn deposits.

2. Geological setting

The Middle–Lower Yangtze River Valley metallogenic belt (MLYRB), located on the northern margin of the South China block, is a key porphyry-skarn Cu–Fe–Au–Mo polymetallic ore belt in China (Fig. 1; Pan and Dong, 1999; Mao et al., 2011; Zhang et al., 2017b,c; Zhang et al., 2018a). The MLYRB is bounded by the Xiangfan-Guangji Fault (XGF) in the northwest, by the regional strike-slip Tancheng-Lujiang Fault (TLF) in the northeast, and by the Yangxin-Changzhou Fault (YCF) in the south (Fig. 1). Stratigraphic sequence in the MLYRB includes a pre-Sinian metamorphic basement, Sinian clastic rocks and dolomite, Cambrian to Triassic pelagic carbonates and Jurassic-Cretaceous continental arc volcanic rocks with clastic interbeds. Triassic pelagic carbonates are important ore host for the MLYRB skarn deposits (Mao et al., 2011). In the belt, the Late Jurassic-Cretaceous calc-alkaline intrusions and Early Cretaceous (sub)-alkaline volcanic rocks (Chen et al., 2001; Xie et al., 2006) can be divided into three magmatic phases (Fig. 1): 156 to 137 Ma high-K calc-alkaline granitoids (diorite, granite, granodiorite and granodiorite porphyry in the uplifted blocks); 135 to

123 Ma Na-rich calc-alkaline granitoids (gabbro, pyroxene diorite, quartz diorite, quartz-monzonite, granodiorite, granite, and diorite-granodiorite porphyries); 135 to 123 Ma A-type granites (Mao et al., 2011). There are seven ore districts in the MLYRB belt, i.e., (from west to east) the Edong, Jiurui, Anqing-Guichi, Luzong, Tongling, Ningwu and Ningzhen districts (Fig. 1), containing over 200 polymetallic deposits (Pan and Dong, 1999; Mao et al., 2006; Zhou et al., 2012).

The Edong ore district, in the westernmost section of the MLYRB, is situated in southeastern Hubei province (Fig. 1). In this district, the Neoproterozoic metamorphic rocks are poorly exposed (Mao et al., 2011), whereas the Cambrian to Middle Triassic pelagic carbonate and clastic rocks are widely exposed in southern Edong (Fig. 2a). The Cretaceous Lingxiang Formation volcanic rocks (mainly andesitic basalt), the Majiashan Formation volcanic breccias and the Middle Triassic Puqi Formation clastic rocks (mudstone and siltstone) are exposed in western Edong (Mao et al., 2011). The Jinniu basin in western Edong contains rhyolite, basalt, basaltic andesite, and trachytic basalt, andesite and dacite (Xie et al., 2006; Mao et al., 2011). Around the southern Jinniu basin, there are also Upper Triassic to Middle Jurassic clastic rocks (Fig. 2a).

There are six granitic batholiths in the Edong district, namely (from north to south) Echeng, Tieshan, Jinshandian, Lingxiang, Yinzu and Yangxin (Fig. 2a; Shu et al., 1992). The batholiths in the north (Echeng, Tieshan and Jinshandian) are mainly Fe skarn related (e.g., Chengchao Fe, Jinshandian Fe and Tieshan Fe–Cu deposits). The Echeng batholith (zircon U–Pb age: 143 ± 2 Ma to 127 ± 2 Ma; Xie et al., 2011; Xie et al., 2012) comprises quartz diorite and granite, whilst the Tieshan batholith comprises quartz diorite (142 ± 3 Ma), gabbro (137 ± 2 Ma), and biotite diorite (136 ± 2 Ma) (Li et al., 2009b; Xie et al., 2011). The Jinshandian batholith comprises granite (133 ± 1 Ma) and quartz diorite (127 ± 2 Ma) (Xie et al., 2012). The batholiths in the south (Lingxiang and Yangxin) are mainly Cu–(Au) skarn related (e.g., Jiguanzui Cu–Au and Tonglvshan Cu–Fe deposits) (Fig. 2b; Xie et al., 2009; Mao et al., 2011). The Lingxiang batholith (146 ± 1 Ma and 142 ± 1 Ma; Li et al., 2010; Xie et al., 2011) comprises gabbro, quartz diorite and granodiorite, whilst the Yangxin batholith (142 ± 1 Ma to 134 ± 2 Ma; Li et al., 2009b; Li et al., 2010; Xie et al., 2011) comprises quartz diorite, granite and monzonite. The Yinzu batholith (also in southern Edong but only associated with very few deposits) comprises diorite and granodiorite-porphyry (152 ± 2 Ma and 146 Ma; Li et al., 2009b; Li et al., 2010).

3. Deposit geology

The Jiguanzui Cu–Au skarn deposit is located in the central Edong. The sedimentary rocks that crop out at Jiguanzui are the Lingxiang (Cretaceous volcanic rocks), Majiashan (Cretaceous volcanic breccia), Puqi (Middle Triassic clastic rocks) and Jialingjiang (Middle to Early Triassic dolomitic marble) formations, among which Jialingjiang Formation is the main ore-hosting strata. Major structures at Jiguanzui
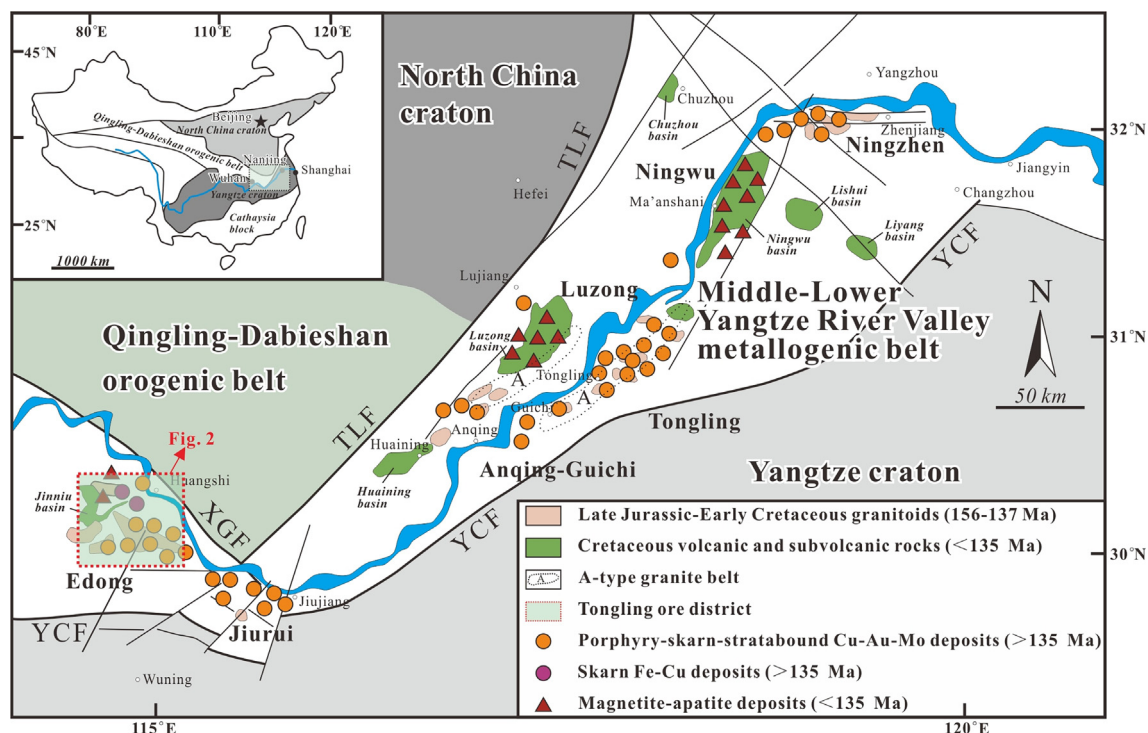
Fig. 1. a. Schematic map showing the location of the Middle–Lower Yangtze River Valley metallogenic belt (MLYRB) (modified after Mao et al., 2011). b. Sketch map showing the distribution of porphyry related, skarn and stratabound Cu–Au–Mo–Fe deposits (> 135 Ma), magnetite–apatite and Fe skarn deposits (< 135 Ma) and their associated granitoids and Cretaceous volcano-sedimentary basins along the MLYRB (modified after Mao et al., 2011; Zhang et al., 2017a–c). XGF: Xiang-fan–Guangji fault, TLF: Tancheng–Lujiang fault, YCF: Yangxing–Changzhou fault.
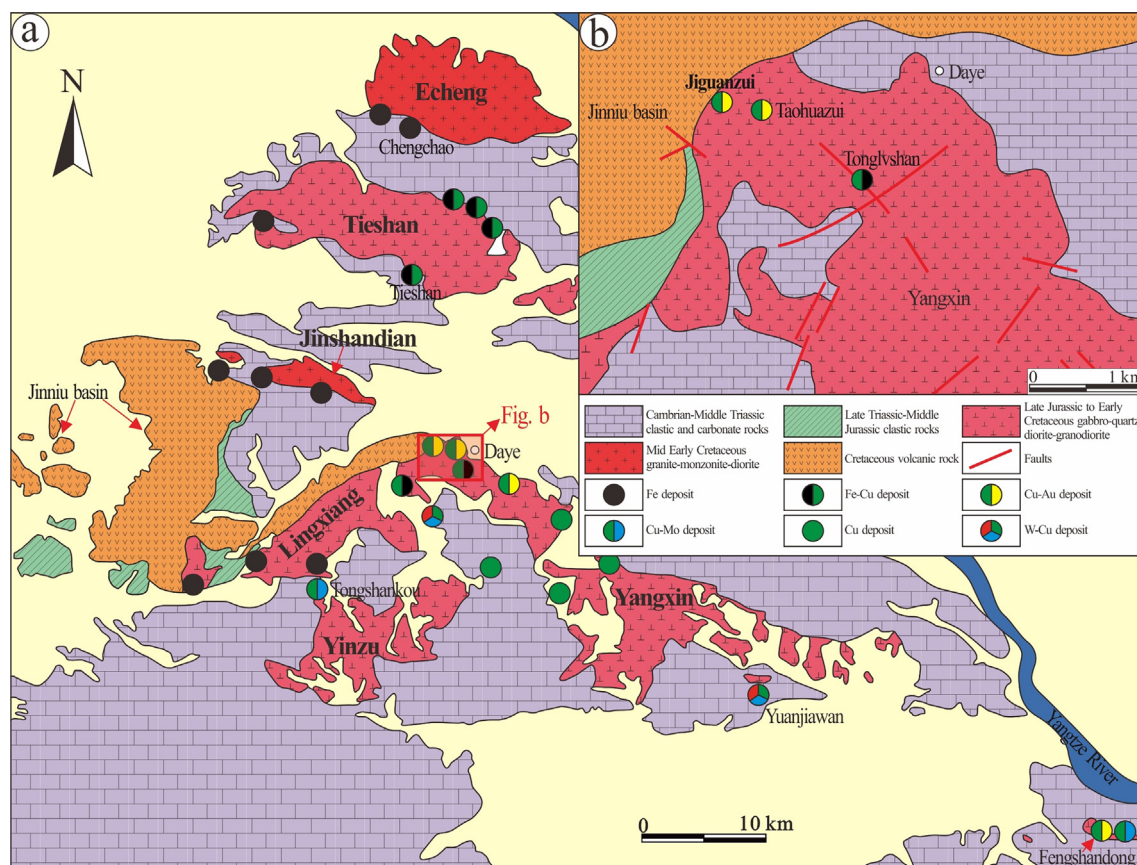

Fig. 2. a. Geologic map of southeastern Hubei in the MLYRB, showing the major types of mineral deposits (modified after Shu et al., 1992; Li et al., 2008). b. Geologic map of the Tonglvshan ore district, showing the orebody distribution (modified after Chang et al., 1991; Xie et al., 2009; Mao et al., 2011).
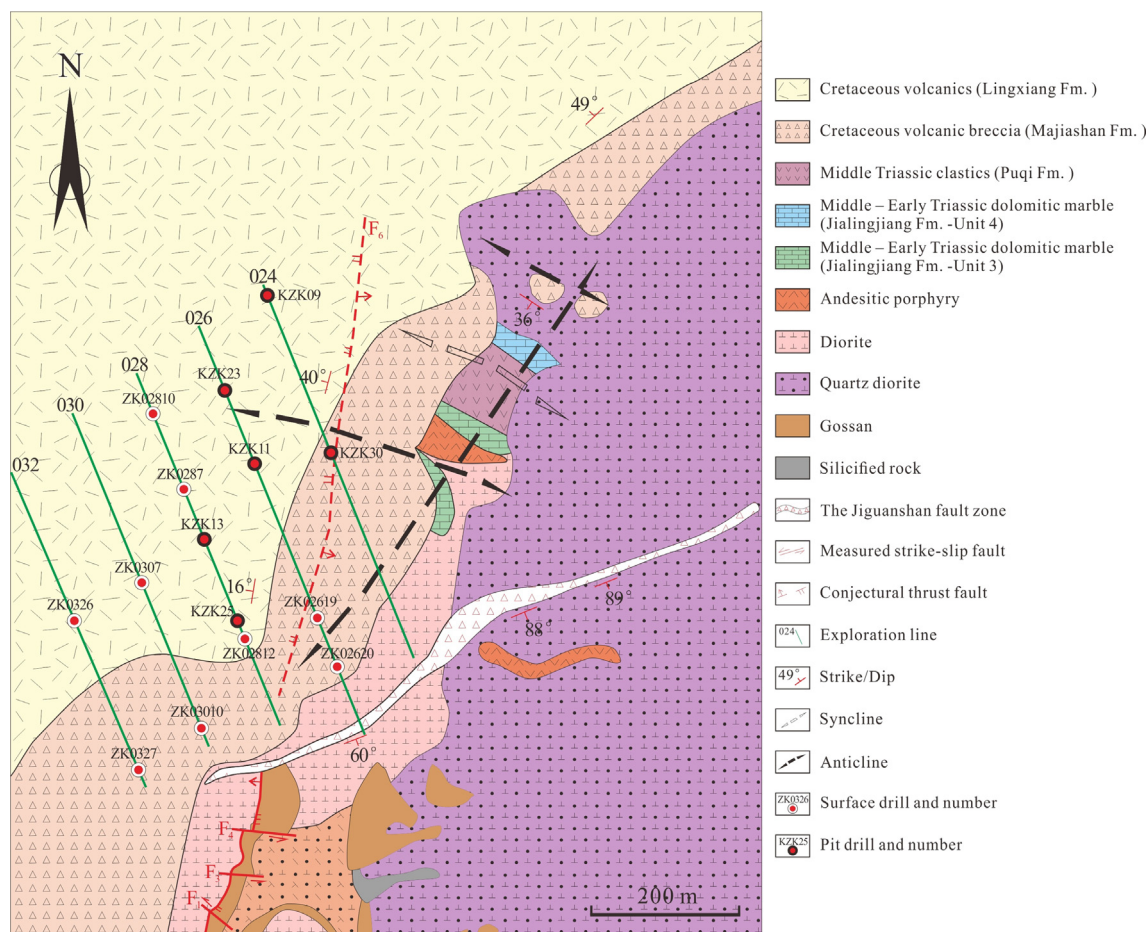
Fig. 3. Geologic map of the Jiguanzui Cu–Au deposit (modified after Ke et al., 2016; Zhang et al., 2016).

are the NE-trending Jiguanshan thrust fault and NW-trending anticlines and synclines. The magmatic rocks in the mining area are part of the Tonglvshan complex, mainly consisting of diorite and quartz diorite with local andesitic porphyry (Fig. 3).

The Jiguanzui deposit has 7 major orebodies (I# to VII#) (Ke et al., 2016; Fig. 4), which occur as stratiform, veins and lenses in the Triassic Jialingjiang Formation dolomitic marble and the Puqi Formation hornfels with mudstone and siltstone protoliths. The I# to III# orebodies occur in the western limb of the concealed NNE-trending anticline. The III # orebody is the largest (670 m long and 1–103 m wide), and is located at 22–531 m deep. The IV# orebody occurs in dolomitic marble xenoliths in the southeast of the concealed anticline with a dip SE of 45°. The lenticular VI# orebody is located in the lower part of the IV # orebody, and dips SE at 60° to 75°. The lenticular VI# orebody is located in the lower part of the III # orebody, and dips NW at 50° to 74°.

4. Mineralization and alteration paragenesis

Based on the detailed field research, systematic microscopic identification and SWIR spectral analyses (TerraSpec, Analytical Spectral Devices, Inc (ASD)), five alteration/mineralization stages were identified at Jiguanzui, namely (I) prograde skarn (garnet-pyroxene) alteration, (II) retrograde (hornblende-epidote-actinolite) alteration, (III) hematite mineralization, (IV) main-stage (quartz-sericite-pyrite-chalcopyrite) mineralization and (V) calcite-sulfide (pyrite-chalcopyrite-molybdenite-galena-sphalerite) mineralization (Fig. 5).

Stage I alteration is dominated by garnet with minor pyroxene (Fig. 5). Garnet occurs as isolated euhedral grains or aggregate with zonal texture (Fig. 6a–c). Pyroxene is mainly euhedral granular, commonly crosscut by late calcite veins (Fig. 6d). Most of the garnets are

replaced by the later minerals, such as epidote, actinolite, hornblende, magnetite and calcite.

Stage II alteration is characterized by abundant hornblende, epidote and actinolite with minor biotite and magnetite (Fig. 5). Stage II minerals are commonly found crosscutting/replacing Stage I garnet and pyroxene, e.g., euhedral hornblende replaced garnet (Fig. 6e), anhedral actinolite replaced garnet with metasomatic relict texture (Fig. 6f), and epidote vein crosscut garnet (Fig. 6g). Locally, magnetite coexists with biotite and actinolite as clumps (Fig. 6h), suggesting that they may have been coeval.

Stage III mineralization is characterized by hematite and K-feldspar with minor biotite and magnetite (Fig. 5). The anhedral hematite aggregates commonly replaced Stage II actinolite + epidote + hornblende, and was replaced by Stage IV and V quartz + calcite + chlorite, showing metasomatic relict texture (Fig. 6i). Besides, hematite and magnetite commonly replaced garnet, showing pseudomorph or metasomatic relict texture (Fig. 6j, k). Anhedral granular K-feldspar is also found replacing garnet (Fig. 6l).

Stage IV mineralization is composed of abundant pyrite, chalcopyrite, sericite (montmorillonite, muscovite and illite) and quartz with minor digenite, chalcocite, molybdenite, chlorite and trace epidote, calcite, native gold and K-feldspar (Fig. 5). Pyrite is present in many different assemblages: 1) pyrite + chlorite (Fig. 7a); 2) pyrite + quartz + chalcopyrite (Fig. 7b); 3) pyrite + quartz + muscovite (Fig. 7c); 4) pyrite + quartz + epidote + muscovite + illite (Fig. 7d) and 5) pyrite + quartz + biotite + muscovite (Fig. 7e). Among these assemblages, quartz-pyrite-chalcopyrite veins (Fig. 7f) is the main ore host. Sericite is widely distributed with quartz, pyrite, epidote, calcite and biotite as clumps (Fig. 7c–e). Besides, muscovite + illite also occurs as clumps (Fig. 7g) or flakes with fine quartz in
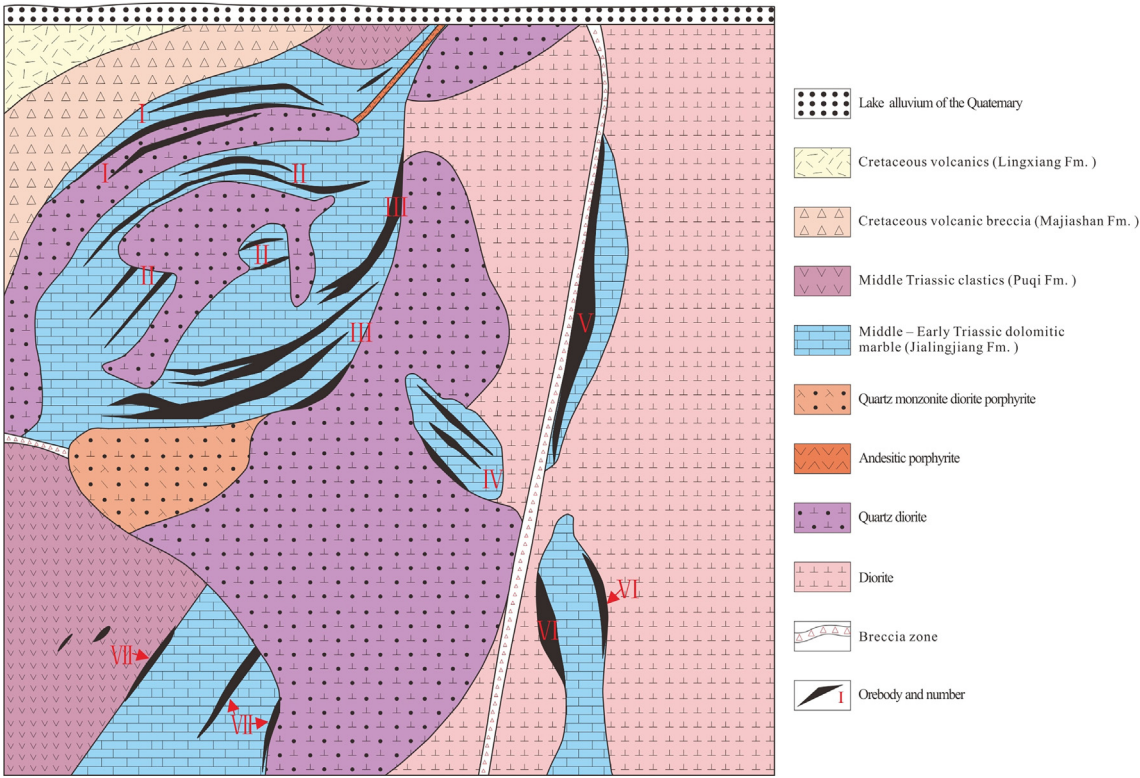
Fig. 4. Sketch map of orebodies of the Jiguanzui Cu–Au deposit (modified after Ke et al., 2016).
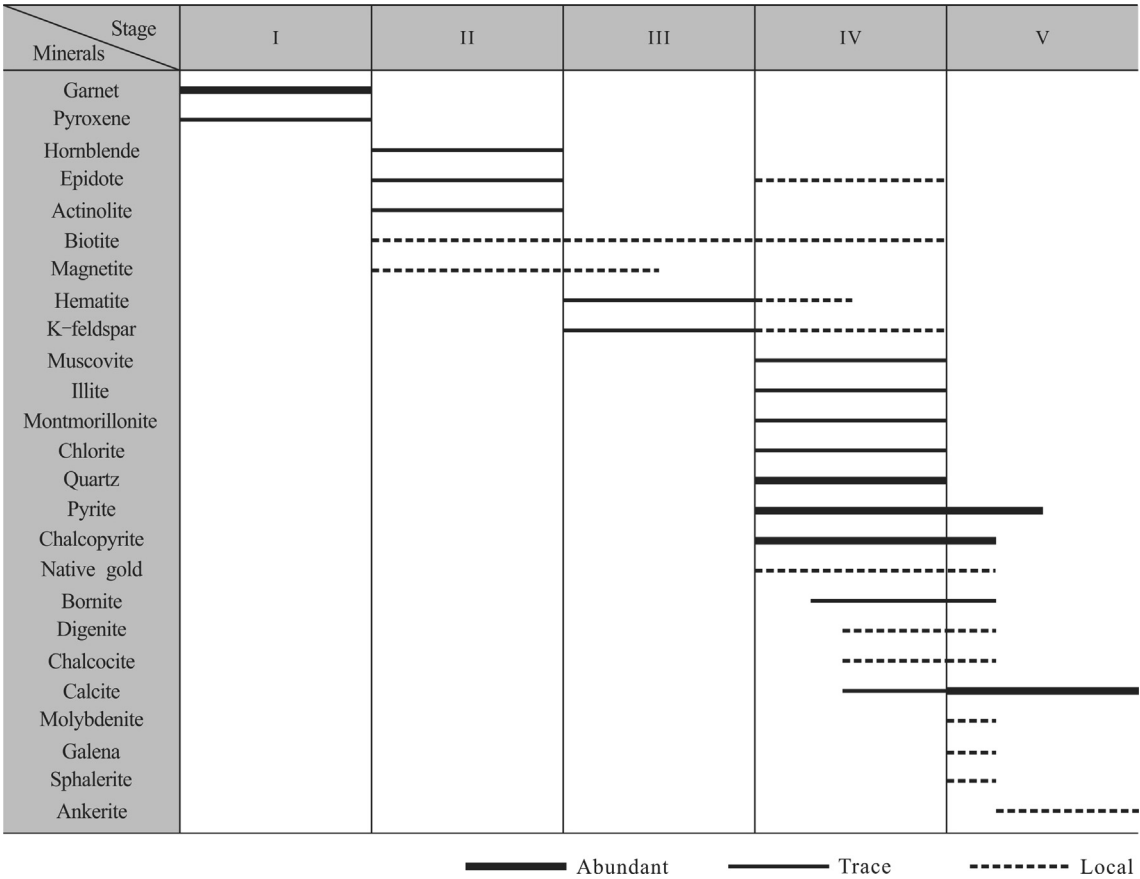
Legend:
- Lake alluvium of the Quaternary
- Cretaceous volcanics (Lingxiang Fm.)
- Cretaceous volcanic breccia (Majiashan Fm.)
- Middle Triassic clastics (Puqi Fm.)
- Middle – Early Triassic dolomitic marble (Jialingjiang Fm.)
- Quartz monzonite diorite porphyrite
- Andesitic porphyrite
- Quartz diorite
- Diorite
- Breccia zone
- Orebody and number

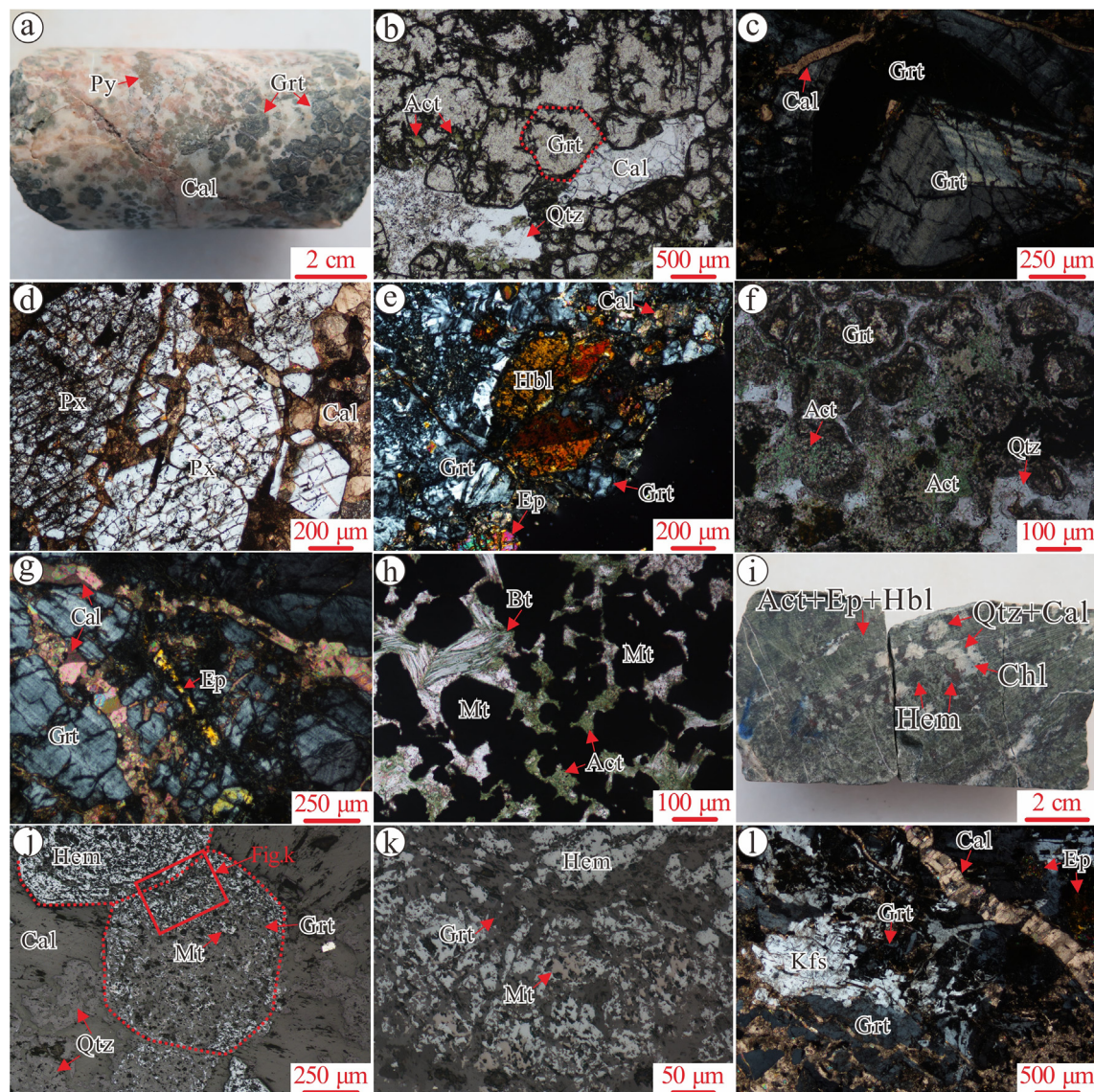**Fig. 5.** Paragenetic sequence of the Jiguanzui Cu–Au deposit.

Fig. 6. Photographs and photomicrographs showing the alteration/mineralization Stage I– III of the Jiguanzui deposit. a. Garnet occurs as euhedral grains in hand specimen; b. Garnet occurs as aggregates, replaced by actinolite; c. Zonal garnet replaced by calcite vein; d. Pyroxene occurs as euhedral grains, replaced by late calcite veins; e. Hornblende, epidote and calcite replaced garnet; f. Actinolite replaced garnet; g. Epidote and late calcite vein replaced garnet; h. Clump of magnetite + biotite + actinolite; i. Impregnated quartz + calcite + chlorite + hematite replaced actinolite + epidote + hornblende skarn in hand specimen; j. Hematite ± magnetite replaced the garnet; k. Hematite ± magnetite replaced the garnet; l. K-feldspar and late calcite vein replaced garnet. Abbreviations: Act = actinolite, Bt = biotite, Cal = calcite, Chl = chlorite, Ep = epidote, Grt = garnet, Hbl = hornblende, Hem = hematite, Kfs = K-feldspar, Mt = magnetite, Px = pyroxene, Py = pyrite, Qtz = quartz.

the altered wall rock. Native gold occurs as anhedral grains and coexists with bornite and chalcopyrite in pyrite (Fig. 7h).

Stage V alteration/mineralization is characterized by abundant calcite, pyrite and chalcopyrite, with minor ankerite, native gold, bornite, digenite, chalcocite, galena, sphalerite and molybdenite (Fig. 5). Calcite + pyrite + chalcopyrite ± molybdenite veins are common in this stage (Fig. 7i). Chalcopyrite is anhedral and coexists with calcite (Fig. 7j). Few calcite + pyrite + galena veins are locally present (Fig. 7k). Poikilitic native gold occurs in chalcopyrite that coexists with sphalerite (Fig. 7l). Additionally, pyrite locally occurs as vein with calcite or ankerite (Fig. 7m, n), and calcite veins commonly crosscut the pyrite-chalcopyrite ore (Fig. 7o).

5. Sampling and analytical methods

A total of 15 drill holes were selected from 5 exploration lines, i.e., 24# (drill holes KZK09 and KZK30), 26# (drill holes KZK11, KZK23,

ZK02619 and ZK02620), 28# (drill holes KZK13, KZK25, ZK0287, ZK02810 and ZK02812), 30# (drill holes ZK0307 and ZK03010), 32# (drill holes ZK0326 and ZK0327) exploration lines (Fig. 8). We collected 1879 samples from these 15 drill holes, with the sampling locations shown in Fig. 8. Sampling interval was normally about 8.28 m, and decreased where the alteration (intensity or type) and/or mineralization intensify or lithology changes. A total of 398 polished thin sections were prepared for the representative samples, and were studied under the microscope to identify alteration minerals. Based on the microscopic observations, we conducted the SWIR spectral analyses.

Sample preparation for SWIR spectral analyses requires the drill core sample surface to be clean and dry. Three analysis spots were chosen on each sample (to ensure data reliability) and marked. A total of 4, 962 SWIR spectra were obtained from 1, 654 samples (225 samples were discarded due to the presence of large amounts of sulfides) with a TerraSpec device (ASD TerraSpec 4 Hi-Res Mineral Spectrometer). After the instrument was connected, set the parameters
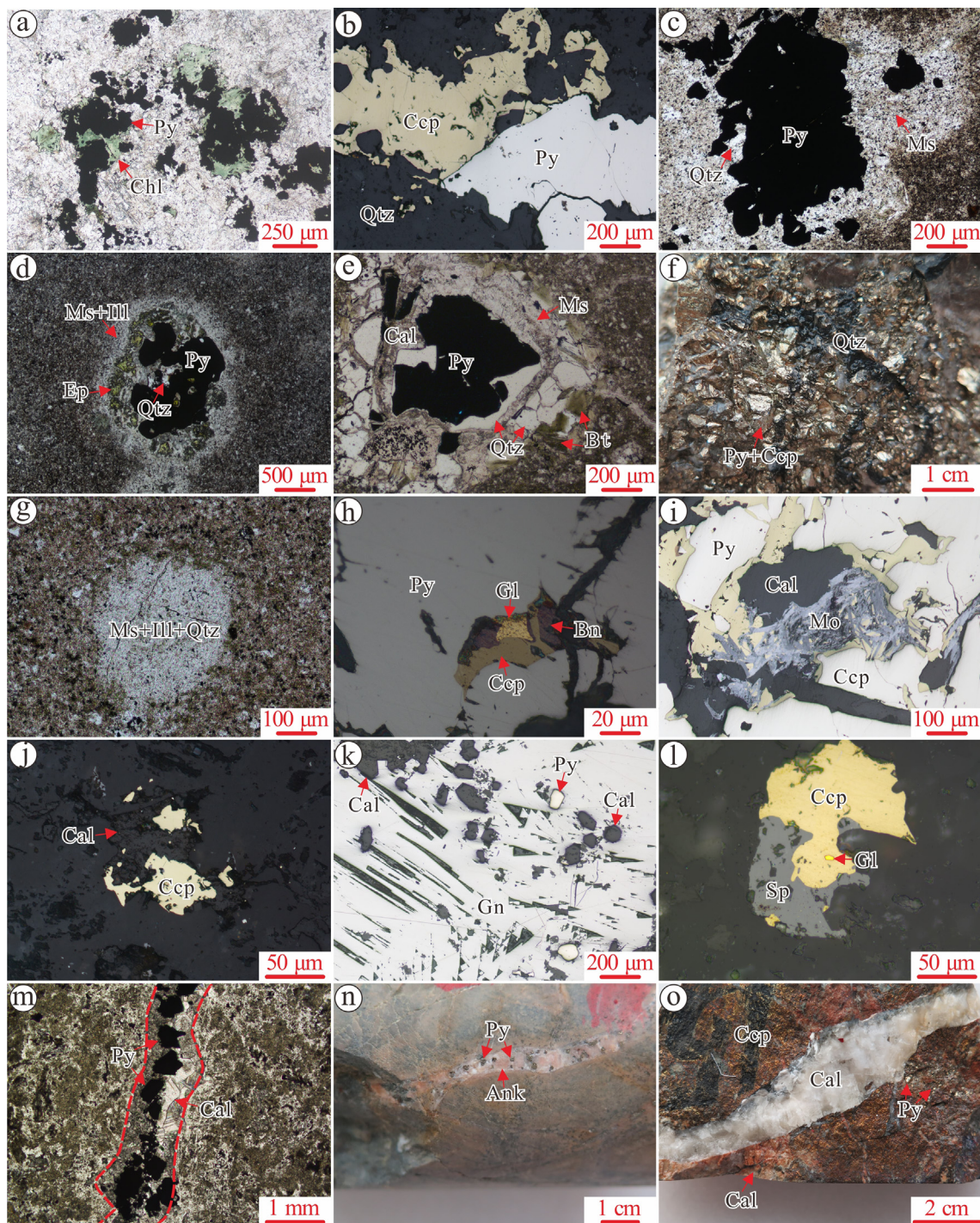
Fig. 7. Photographs and photomicrographs showing the alteration/mineralization Stage IV and V of the Jiguanzui deposit. a. Pyrite + chlorite; b. Pyrite + quartz + chalcopyrite; c. Clump of muscovite + quartz + pyrite; d. Clump of muscovite + illite + quartz + epidote + pyrite; e. Clump of muscovite + quartz + biotite + calcite + pyrite; f. Quartz + pyrite + chalcopyrite ore; g. Clump of muscovite + illite and microcrystalline quartz; h. Anhedral native gold coexists with bornite and chalcopyrite in pyrite; i. Calcite-pyrite-chalcopyrite ± molybdenite vein; j. Clump of calcite + chalcopyrite; k. Calcite-pyrite-galena vein; l. Clump of sphalerite and chalcopyrite with native gold in chalcopyrite; m. Calcite-pyrite vein; n. Ankerite-pyrite vein; o. Calcite vein crosscut quartz-sulfide ores. Abbreviations: Ank = ankerite, Bn = bornite, Bt = biotite, Cal = calcite, Ccp = chalcopyrite, Ep = epidote, Gl = native gold, Gn = galena, Ill = illite, Mo = molybdenite, Ms = muscovite, Py = pyrite, Qtz = quartz, Sp = sphalerite.

in the TerraSpec signal collection software, then instrument optimization and white balance were performed for every 20 min. Detailed instrument parameter settings for the TerraSpec are outlined in Chang and Yang (2012).

The spectral data was automatically processed using The Spectral Geologist (TSG) V.3 software. Mineral identification and its abundance estimation were based on the intensity, wavelength and shape of the main absorption features in each spectrum. The SWIR numerical parameters, including wavelength position and absorption depth of sericite group (montmorillonite, illite and muscovite) Al-OH, and chlorite and carbonate (calcite, ankerite and dolomite) Fe-OH, were extracted using the Scalar function of TSG. Setting for the acquisition
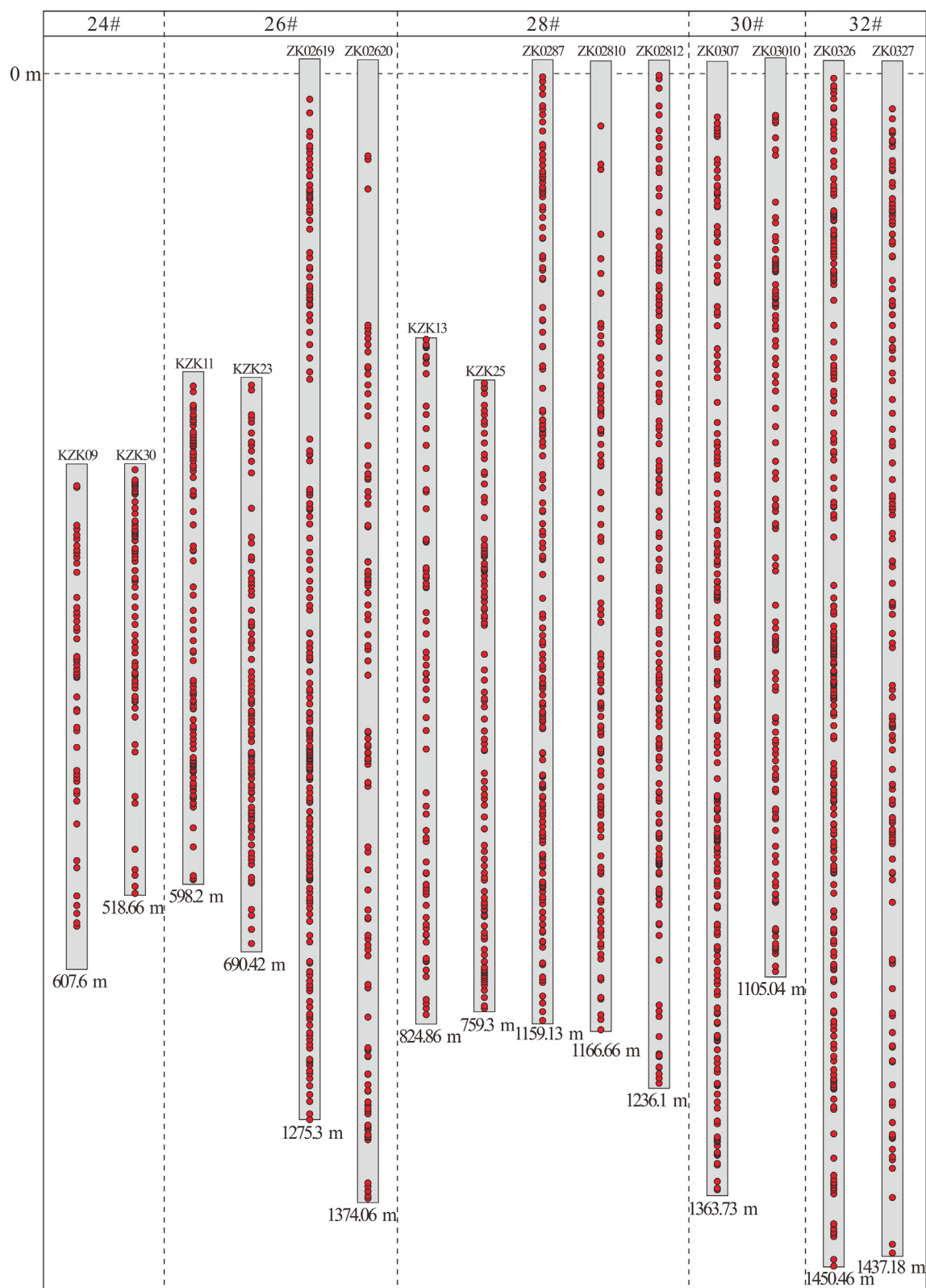
Fig. 8. Diagram of drill core sample distribution in Jiguanzui.

parameters were as outlined in Chang and Yang (2012) and Yang et al. (2012).

Molecular bonds of H_2O, OH, CO_3, NH_4, Al-OH, Fe-OH and Mg-OH have characteristic absorption features in the SWIR bands. Combinations of these absorption features were used to determine mineral groups, e.g., phyllosilicates, carbonates, sulfates, OH-bearing

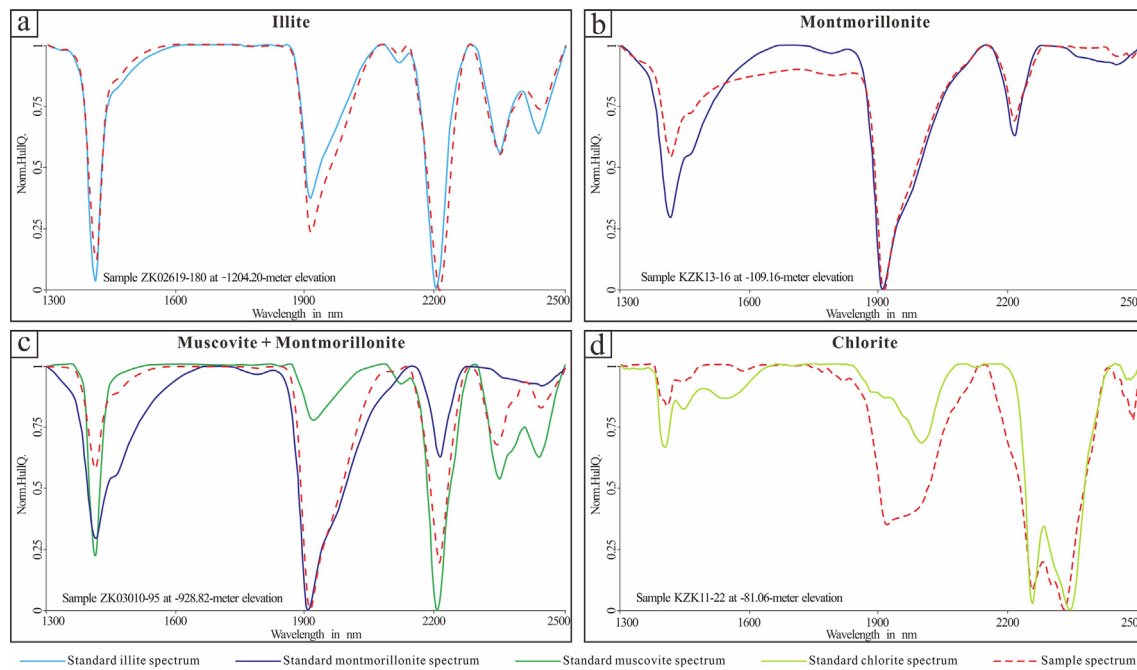and NH_4-bearing minerals (Thompson et al., 1999; Jones et al., 2005)

Fig. 9. Characteristic spectrum of sericite group minerals (muscovite, illite and montmorillonite) and chlorite. a. Muscovite spectrum in Sample KZK11-34 at −140.20-meter elevation; b. Illite spectrum in Sample KZK13-59 at −669.05-meter elevation; c. Montmorillonite spectrum in Sample KZK13-16 at −109.16-meter elevation; d. Chlorite spectrum in Sample KZK11-22 at −81.06-meter elevation.
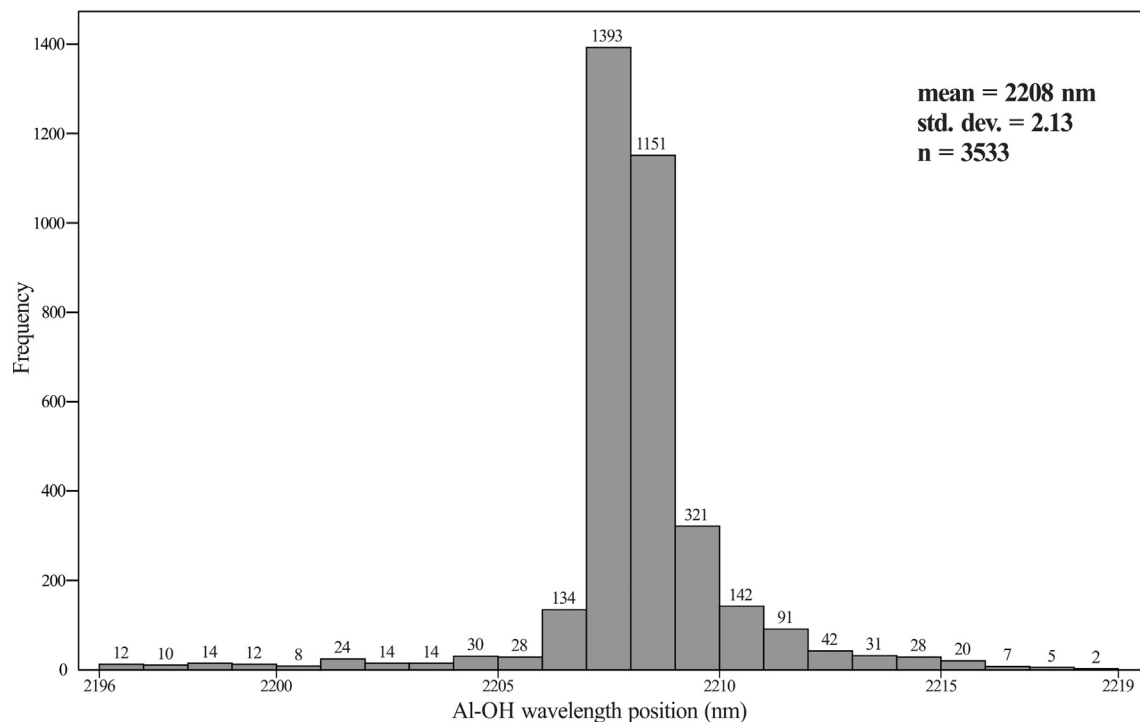

Fig. 10. Frequency distribution histogram of absorption band position for Al-OH absorption.

6. Results

6.1. Alteration minerals

Out of the 5637 SWIR spectra obtained from Jiguanzui, 675 spectra were discarded due to their low signal-to-noise ratios. The average of the three values obtained from each sample represents the spectral eigenvalue. The results suggest the presence of sericite group minerals (montmorillonite, illite and muscovite), kaolinite, halloysite, dickite, chlorite and carbonate minerals (calcite, ankerite and dolomite). A total of 2893 spectra show only a single mineral, e.g., montmorillonite, illite, muscovite, kaolinite, halloysite, calcite and dolomite, whilst the rest show two or more minerals, e.g., montmorillonite + halloysite, montmorillonite + kaolinite, montmorillonite + calcite, illite + calcite.

The results show that the Al-OH absorption feature is mainly associated with sericite group minerals, whilst the Fe-OH absorption feature is associated with chlorite and carbonate minerals. Sericite group minerals are the most common alteration minerals in most alteration
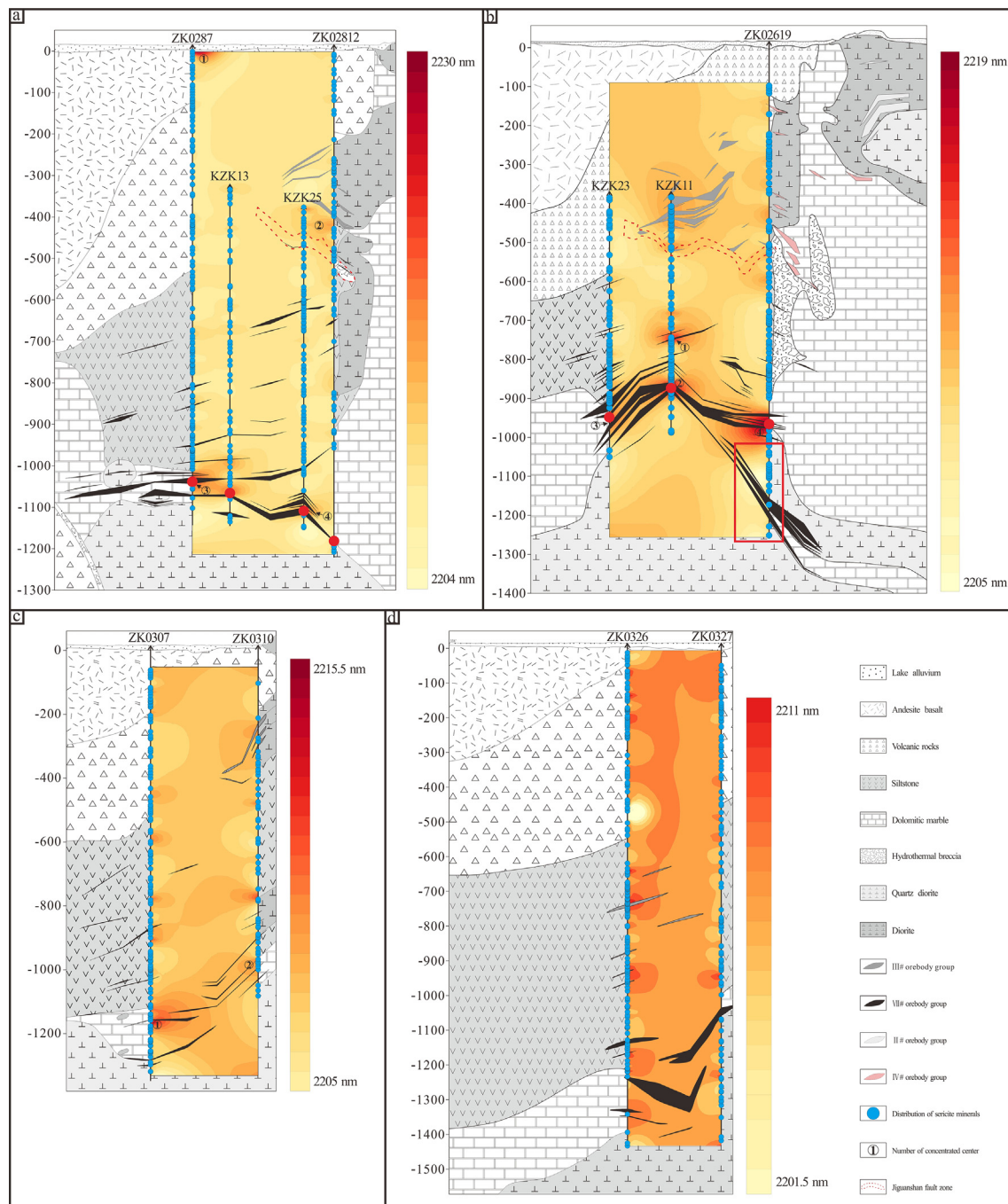
Fig. 11. Color gradient map of the Al-OH absorption feature wavelength position in Jiguanzui (a) 28# line; (b). 26# line; (c). 30# line; (d). 32# line.

zones at Jiguanzui (except for the main mineralization zone). Muscovite and illite have sharp, deep, single Al-OH absorption features of 2196–2215 nm and 2196–2223 nm, respectively, and weaker secondary Al-OH absorption features near 2344 and 2400 nm (Herrmann et al., 2001; Jones et al., 2005; Chang and Yang, 2012; Fig. 9a). Montmorillonite has a wide, shallow, single Al-OH absorption feature of 2190–2227 nm (Fig. 9b). Sericite group minerals show generally good zonation, i.e., (from top to bottom of drill hole) montmorillonite → illite ± montmorillonite → muscovite ± montmorillonite. Some illite and muscovite show varying degrees of mixing with halloysite or montmorillonite (Fig. 9c).

Chlorite spectra has Fe-OH and Mg-OH absorption features near 2255 nm (ranging 2240–2270 nm) and 2335 nm (ranging 2315–2355 nm), respectively (Fig. 9d). SWIR analyses show that the

intensity of chlorite alteration is lower than sericite alteration at Jiguanzui as only 154 SWIR spectra contain chlorite, among which 31 spectra contain only chlorite, and the rest contain chlorite and mostly montmorillonite and/or kaolinite, and less commonly illite, halloysite and/or dolomite. Carbonates have diagnostic CO_3 absorption features of 2300–2350 nm, which overlap with those of Mg-OH and secondary Al-OH (Huang et al., 2018). A total of 1535 SWIR spectra contain carbonates (calcite, dolomite and ankerite), among which 472 contain only one carbonate mineral. The rest contain carbonate and mostly montmorillonite and/or kaolinite, and less commonly dickite, halloysite, chlorite and/or gypsum.
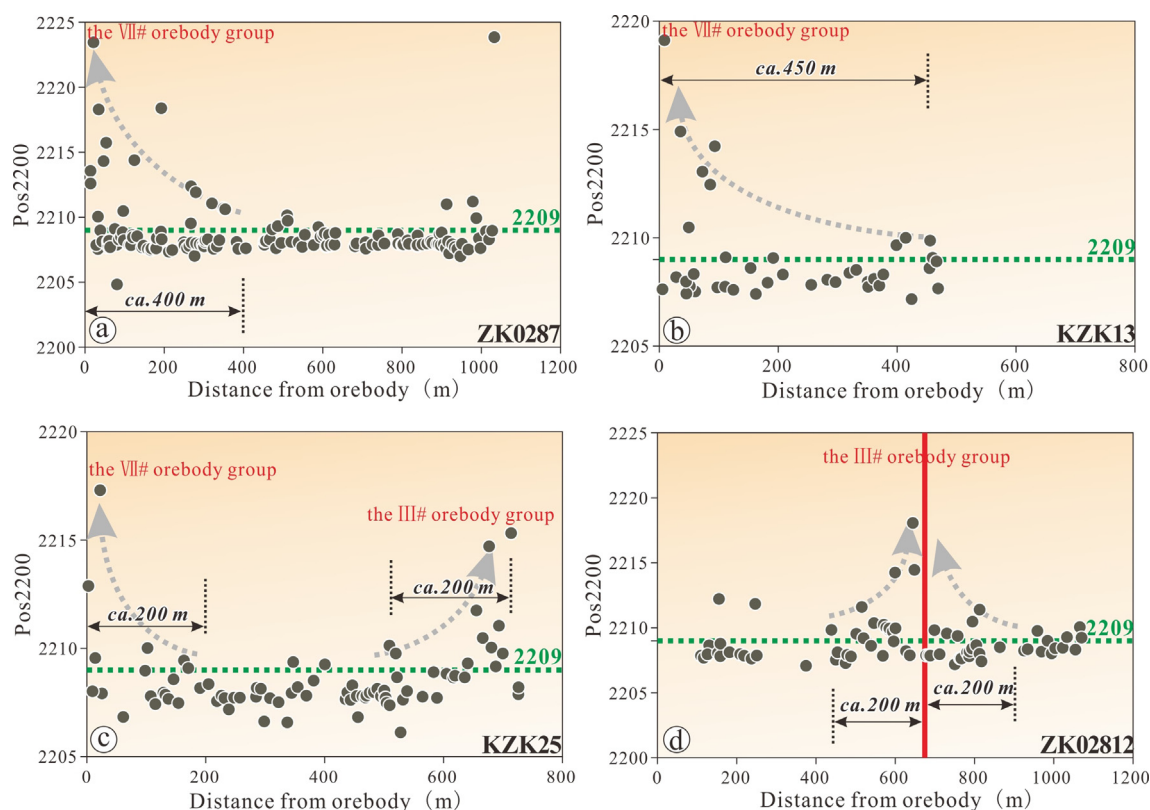
Fig. 12. Scatter diagram of distance from orebody with the Al-OH absorption feature wavelength position in the 28# exploration line in Jiguanzui Cu–Au deposit.

6.2. Spectral features

6.2.1. Sericite group minerals

At Jiguanzui, the Al-OH absorption feature of sericite group minerals were found in 3533 SWIR spectra (62.7% of the total). The wavelength covers a range from 2196 to 2219 nm, with most values clustering in 2206–2212 nm (mean = 2208, median = 2208 nm, n = 3533) (Fig. 10). In this study, the sampling interval is similar in each drill hole, but the spacing of drill holes in each exploration line is different, with the 28# line being the shortest. Therefore, this study mainly focused on the 28# line for the discussion on the relationship between the Al-OH absorption features and the VI # orebody, whilst taking other exploration lines as verification.

The sericite Al-OH absorption feature wavelength position (Pos2200) does not change obviously in the 28# line (the wavelength range is 2204–2230 nm), and are clustered in four centers (with the Kriging method by using Surfer 12.2, Golden Software Corporation) (Fig. 11a). Center No. 1 is located near 0-meter elevation in ZK0287, not directly coupled with any orebodies. Center No. 2 is located between ZK02812 and KZK25 at −400-meter elevation. The center is located in the contact zone between quartz diorite and hornfels, and the occurrence is nearby the III # orebody. Center No. 3 is located in the contact zone between quartz diorite and marble near −1050-meter elevation in ZK0287. This center spatially overlap with the VI # orebody. Center No. 4 is located in the quartz diorite-marble contact zone near −1100-meter elevation in KZK25. Although this center is relatively small, it closely overlaps with the VI # orebody. Overall, the centers of Pos2200 spatially coincide well with the orebodies in the 28# line.

In order to further verify the coupling of the Al-OH absorption features of the sericite group minerals with other orebodies in Jiguanzui, the Pos2200 of 26#, 30# and 32# lines are selected for comparison. There are four clear centers of Pos2200 in the 26# line which spatially coincide with the orebodies (Fig. 11b). In addition, the

area at −500 to −350-meter elevation in KZK11 do not form a clear center, but the Pos2200 remains high for sericite group minerals, which shows good coupling with the III # orebody. The Pos2200 of the 30# line also shows several distinct centers that spatially coincide with the orebodies (Fig. 11c). However, the characteristic values of Pos2200 are generally high and no clear center can be identified in the 32# line (Fig. 11d).

To better illustrate the relationship between Pos2200 and orebody location, we chose the mineralization centers intersected in each drill hole (red circles in Fig. 11a, b), and plotted the scatter diagram of distance from the mineralization centers versus the position of Al-OH absorption feature wavelength in the 28# and 26# lines (Figs. 12 and 13; Supplementary Appendix 1). Figs. 12 and 13 show that the lower limit of the Pos2200 that could indicate the orebody is 2209 nm both in the 28# line and 26# line. But the distance from the orebody that could be indicated is different. In the 28# line, the distance that could indicate the VI # orebody is about 400 m (in ZK0287) and 450 m (in KZK13) (Fig. 12a, b). However, the distance (indicated the III # and VI # orebodies) in KZK25 is only about 200 m (Fig. 12c), and the distance that could indicate the III # orebody is also about 200 m in ZK02812 (Fig. 12d). In the 26# line, the indicating distance for VI # orebody in KZK23 is 400 m (Fig. 13a), and the indicating distance in KZK11 is 230 m (for VI # orebody) and 100 m (for III # orebody) (Fig. 13b). The indicating distance in ZK02619 for VI # orebody is about 200 m (Fig. 13c).

6.2.2. Chlorite

In porphyry and VMS deposits, the Fe-OH absorption feature of chlorite has good indication for hydrothermal and mineralization center by chlorite Fe-OH absorption feature wavelength position (Pos2250) (Herrmann et al., 2001; Sun et al., 2001; Jones et al., 2005; Yang et al., 2005; Biel et al., 2012; Laakso et al., 2015, 2016; Xu et al., 2017; Huang et al., 2018; Neal et al., 2018), yet any indication by the chlorite Fe-OH absorption on skarn deposits is still unclear. At
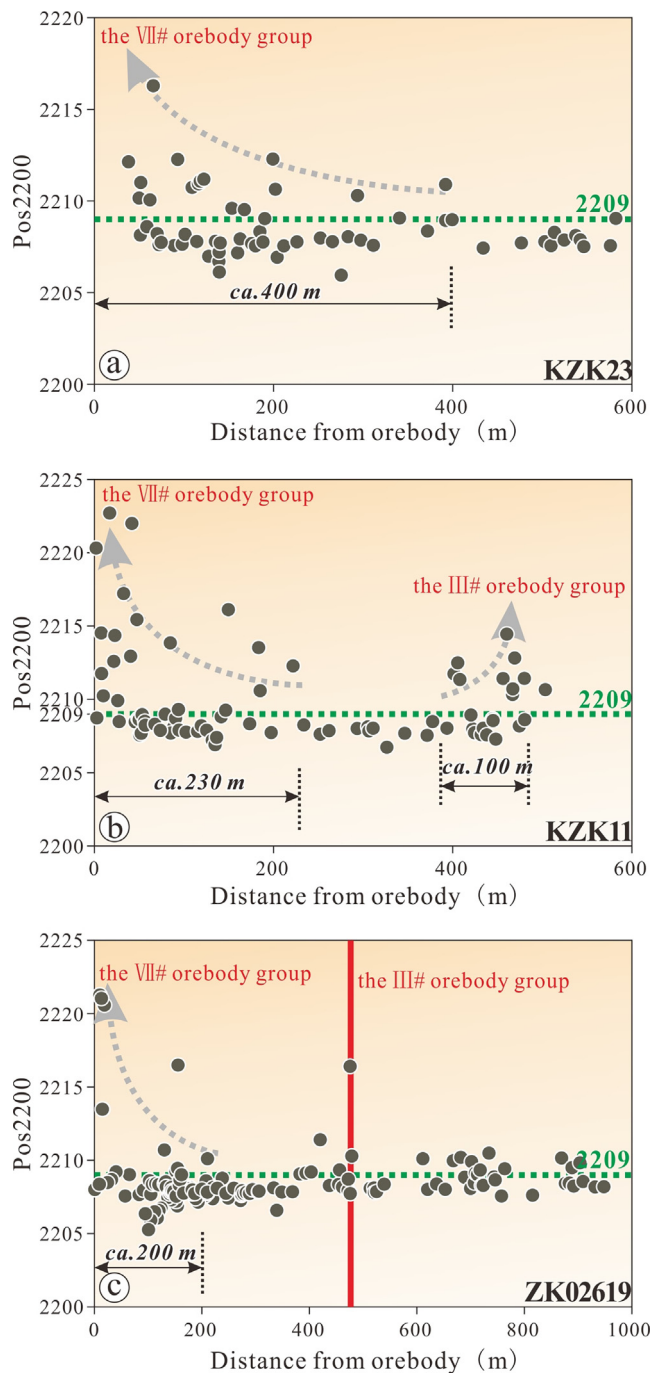
Fig. 13. Scatter diagram of distance from orebody with the Al-OH absorption feature wavelength position in the 26# exploration line in Jiguanzui Cu–Au deposit.

Jiguanzui, 154 SWIR spectra of chlorite were collected (only 2.7% of the total). Since part of the Mg-OH absorption feature is similar to carbonates, especially ankerite and dolomite, the chlorite Fe-OH absorption feature is chosen. The wavelength position frequency distribution of the Fe-OH absorption position (Pos2250) ranges 2241–2263 nm, mostly clustering around 2245–2250 nm (mean = 2250, median = 2249 nm, n = 154) (Fig. 14). Since chlorite is less abundant in KZK25 and ZK02812 of the 28# line, we chose the 26# line to show the relationship between the chlorite Fe-OH absorption feature and the VI # orebody.

The Pos2250 of chlorite changes distinctly in the 26# line, which concentrated in four centers (Fig. 15a; Supplementary Appendix 2):

Center No. 1 is located in the quartz diorite or its contact with marble near −400 to −450-meter elevation, showing a close spatial coincidence with the III # orebody. Center No. 2 is located in the quartz diorite between KZK11 and ZK02619 at −1200-meter elevation, shows a close spatial coincidence with the VI # orebody. In addition, the high chlorite Pos2250 values are also concentrated at the −600 and −750-meter elevation in KZK23 with two subsidiary centers (No. 3 and No. 4). These two centers correspond to one or two small ore lenses of the VI # orebody (Fig. 15a). Although four centers can be identified, the chlorite Pos2250 has less indicative capacity than the sericite Pos2200 for the main part of the VI # orebody.

7. Discussion

7.1. Geochemical implications from the sericite and chlorite spectral features

Sericite group minerals account for 62.7% of the total SWIR analyses, and are the most common alteration minerals at Jiguanzui. The majority of sericite group minerals occur in Stage IV, and this stage can therefore be used to verify the relationship with the Jiguanzui deposit orebody in spatial distribution by the SWIR spectral analyses. The wavelength positions of the sericite group mineral Al-OH absorption features display a wide and continuous range (2196–2219 nm). The wide wavelength range (2196–2219 nm) indicates that Al-OH absorption feature may point to the hydrothermal and mineralization center of the mine area (Thompson et al., 1999; Herrmann et al., 2001; Harraden et al., 2013; Tappert et al., 2013; Laakso et al., 2016). And this range is equal to sericite group minerals that span from potassic (2200 to 2208 nm) to phengitic (2216 to 2228 nm) (Herrmann et al., 2001). In Fig. 10, it is shown that the Al-OH absorption wavelength positions were mainly clustered in 2206–2212 nm, which indicates that the sericite group minerals at Jiguanzui are mainly potassic sericite with some phengitic components.

There are two types of Al-OH absorption feature wavelength position variations in different deposits. The first type: in some porphyry and VMS deposits, the most ore-proximal place is characterized by relatively short Al-OH absorption feature wavelength positions, whilst in the ore-distal area the Al-OH wavelength positions shift to long wavelengths (Herrmann et al., 2001; Jones et al., 2005; Yang et al., 2005; Yang et al., 2012; Huang et al., 2018). The second type is just the opposite of the first type (some zinc-lead-silver, VMS and porphyry deposits): Al-OH absorption feature wavelength positions shift to shorter wavelengths from the most ore-proximal to the ore-distal area (Sun et al., 2001; Laakso et al., 2015, 2016; Xu et al., 2017). In this study, the Jiguanzui sericite group minerals in the ore-proximal area have relatively long Al-OH wavelength positions (> 2209 nm), whereas those in the ore-distal area are relatively short (< 2209 nm; Fig. 11) which is same as the second type variation of Pos2200.

The Al-OH wavelength position values correlate positively with the Fe-Mg contents in sericite group minerals, whereas they correlate negatively with the proportions of octahedral Al and temperature (Post and Noble, 1993; Duke, 1994; Scott and Yang, 1997; Laakso et al., 2015, 2016). As for skarn deposits, the octahedral Al content is reduced by the Fe and Mg in the octahedral site (which increases the sericite Fe-Mg content), and this appears to be the main reason for the shift to higher Al-OH absorption wavelengths in the ore-proximal area (Sun et al., 2001; McLeod et al., 1987; Post and Noble, 1993). At Jiguanzui, the mineralization occurs in the intrusive contact with abundant Fe-rich and Mg-rich skarn minerals. This suggests strong skarn alteration and Fe and Mg can substitute the octahedral Al site, leading to the shift to longer wavelengths of the Al-OH absorption band in the ore-proximal area. Although the temperature near the intrusive contact is higher than the intrusion-distal area in skarn deposits, there is no distinct effect on the shortening of the Al-OH absorption band wavelengths at Jiguanzui.

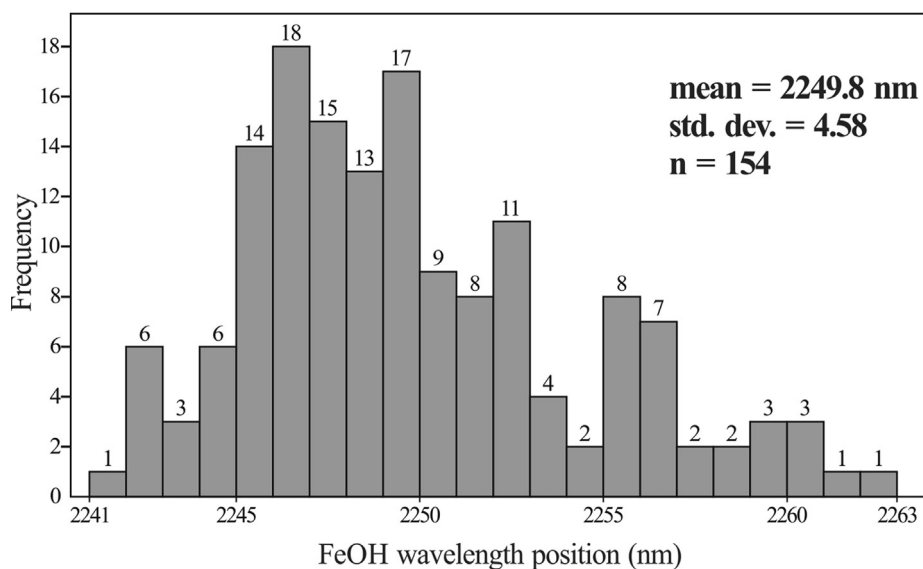The occurrence of Center No. 1 of Al-OH wavelength positions in the

Fig. 14. Frequency distribution histogram of absorption band position for Fe-OH absorption.

0-meter elevation in ZK0287 (Fig. 11a) can be explained by that low-temperature weathering of volcanic rocks led to the reduction of octahedral Al content. In Fig. 11b (the red frame), there is no focusing center of Al-OH absorption position in the −1050 to −1250-meter elevation in ZK02619, but Center No. 2 of Fe-OH wavelength positions was found. This may be caused by the concentration of chlorite and other Fe-rich and Mg-rich skarn minerals (Fig. 15).

As for chlorite, previous SWIR analyses of chlorite suggested good indicative capacity for mineralization center in porphyry and VMS deposits by Pos2250 (Yang et al., 2005; Jones et al., 2005; Biel et al., 2012; Laakso et al., 2015, 2016; Huang et al., 2018; Neal et al., 2018). In this study, the wavelength positions of the Fe-OH absorption features of chlorite span across 2241–2263 nm, clustering in 2245–2253 nm (Fig. 14). Previous studies showed that the Fe-OH absorption feature vary with composition, and that of Mg-rich chlorite is shorter than Fe-rich one (Pontual et al., 1997; Herrmann et al., 2001; Jones et al., 2005). Therefore, the wavelength range measured in this study (2241–2263 nm) corresponds to almost the whole compositional spectrum from Mg-rich to Fe-rich chlorite (2238–2255 nm) (Jones et al., 2005).

In some porphyry and VMS deposits (e.g., Myra Falls and Izok Lake in Canada; Tongshankou in China), the Fe-OH absorption feature wavelengths of chlorite decrease from ore-proximal to ore-distal area (Jones et al., 2005; Laakso et al., 2015; Han et al., 2018; Neal et al., 2018). Yet the case for skarn deposits is largely unreported, only at Tonglvshan (China), Pos2250 shift to shorter wavelengths from the most ore-proximal to the ore-distal area (Zhang et al., 2017a). Similarly, the Fe-OH absorption feature wavelengths become shorter from ore-proximal to ore-distal area at Jiguanzui (Fig. 15a), which may have been associated with the chlorite compositional change from Mg-rich to Fe-rich away from the mineralization center (McLeod et al., 1987; Jones et al., 2005; Laakso et al., 2015; Zhang et al., 2017a; Han et al., 2018; Neal et al., 2018). Xiao et al. (2018a,b) also suggested that chlorite from the propylitic zone at the Tuwu porphyry Cu deposit (Eastern Tianshan, NW China) is Mg-rich and Fe-poor. However, there aren't longer Fe-OH absorption feature wavelengths occur near the main VI # orebody, which may be explained by the lower abundance of chlorite (the blue circles on Fig. 15a).

7.2. Constraints on orebody indications at Jiguanzui

As mentioned above, the long Al-OH absorption feature wavelengths of sericite group minerals at Jiguanzui have potential to indicate skarn mineralization. This is similar to the Hellyer VHMS deposit in Australia (Yang et al., 2011) and the Arroyo Rojo VMS deposit in Argentina (Biel et al., 2012). However, the indication distance of mineralization varies in different drill holes, e.g., 400 m (in ZK0287), 450 m (in KZK13) and 400 m (in KZK23) from the VI # orebody (Figs. 11a–b, 12a), which is because the lithology is single (almost siltstone) within the indication distance. The indication distance is shorter in KZK25 (200 m), KZK11 (230 m) and ZK02619 (200 m) (Figs. 12c, 13b–c), which is probably because: 1) the III # orebody is distributed in the shallow part of these drill holes which affects the vertical indication distance for the VI # orebody; 2) the Jiguanshan fault may have shortened the indication distance from the VI # orebody (red dashed zone in Fig. 11a, b); 3) the rock types above the VI # orebody is variable, including volcanic rocks, siltstone, hydrothermal breccia, quartz diorite and diorite.

Zhang et al. (2017a) pointed out that the chlorite Fe-OH absorption feature wavelength position (Pos2250) shift to shorter wavelengths from the most ore-proximal to the ore-distal area in Tonglvshan skarn deposit in China. Similarly, the Fe-OH absorption feature wavelengths become shorter from ore-proximal to ore-distal area at Jiguanzui (Fig. 15a), but because of the lower abundance of chlorite, it is not obvious in local area (the blue circles on Fig. 15a). At Jiguanzui, sericite group minerals in the ore-proximal area have relatively long Al-OH wavelength positions, whereas those in the ore-distal area are relatively short, and it is similar to Tonglvshan skarn deposit (Zhang, 2018b). In Niancun porphyry deposit, Tibet, the illite crystallinity (IC, IC = Dep2200/Dep1900) is relatively higher (> 1.6) in the eastern portion of the district which was identified as the mineralization/hydrothermal center (Yang et al., 2012). Xu et al. (2017) also pointed out that the IC values showed strong decreasing gradients moving from the mineralized center to the distal barren area in the Xinan Cu–Mo porphyry deposit in China. But the IC indication is not obvious at both Jiguanzui and Tonglvshan (Zhang et al., 2017a; Zhang, 2018b), which is probably caused by interfering of Dep2200 due to abundant other Al-OH contained minerals (such as kaolinite group) coexisting with sericite group minerals in skarn systems. Therefore, we infer that SWIR spectral analyses can be applied to the prospecting of the skarn deposits, and the chlorite and sericite group minerals can be used as possible indicator minerals in skarn deposits with SWIR spectral analyses, however, other SWIR indicators, such as IC values, may be not suitable for exploration criteria to vector the mineralization center and should be applied on caution.
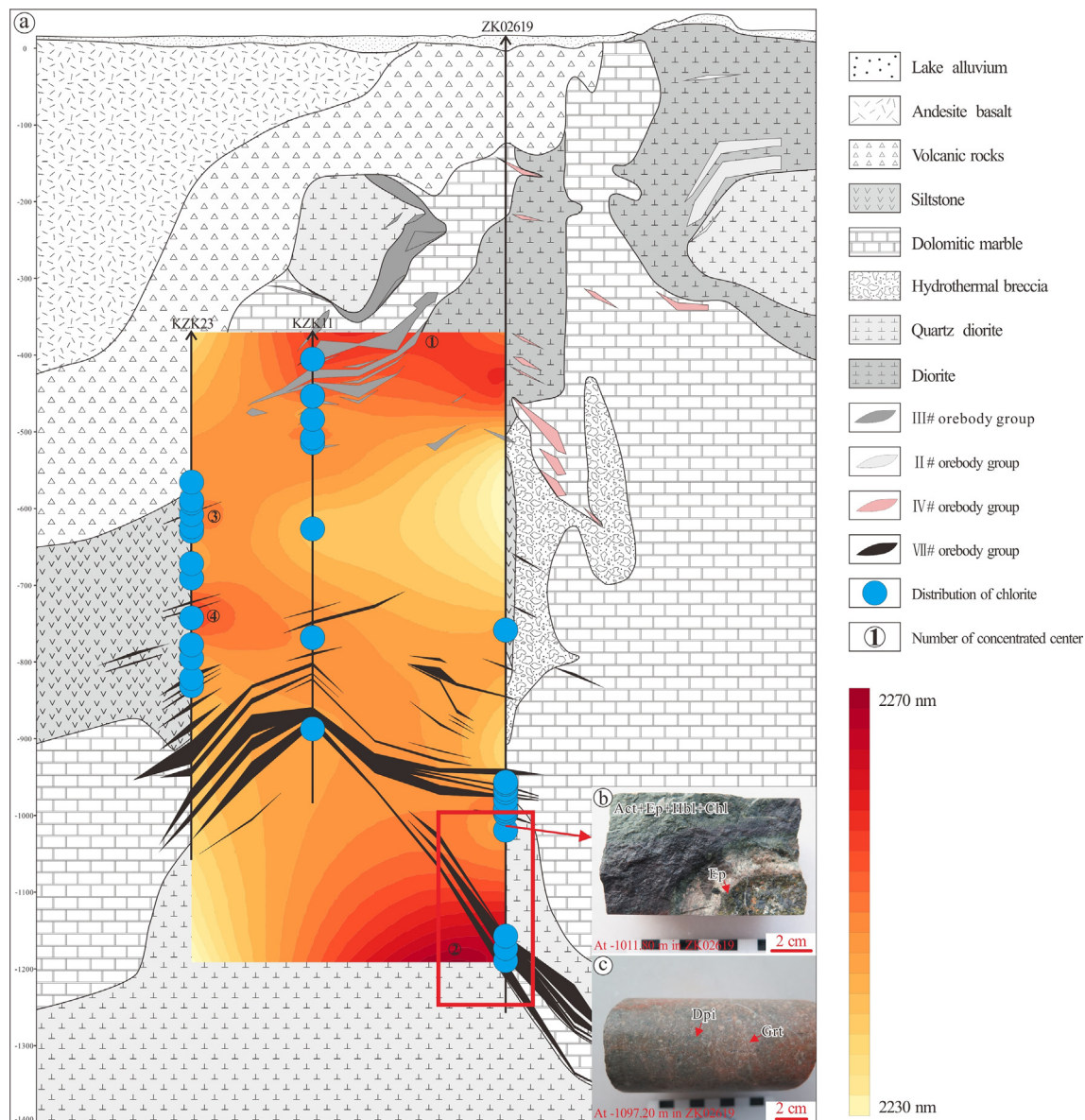
Fig. 15. a. Color gradient map of the Fe-OH absorption feature wavelength position in 26# exploration line in Jiguanzui Cu–Au deposit. b, c. Characteristic photographs showing the strong skarn alteration around the VI # orebody.

8. Conclusions

The Jiguanzui alteration/mineralization can be divided into five stages, namely (I) prograde skarn alteration, (II) retrograde alteration, (III) hematite mineralization, (IV) main-stage mineralization and (V) calcite-sulfides mineralization.

The high Pos2200 area at Jiguanzui often spatially coincides with the orebody location. In local area, the chlorite Fe-OH absorption feature (2241–2263 nm) wavelengths become shorter from ore-proximal to ore-distal area at Jiguanzui. The minimum Al-OH absorption feature wavelength position that could indicate the orebody at Jiguanzui is about 2209 nm, which can be used as a useful vectoring tool at Jiguanzui. Therefore, SWIR spectral analyses may be effective and rapid in identifying alteration minerals and locating hydrothermal centers for skarn deposits.

Acknowledgements

Appendix A. Supplementary data

Supplementary data to this article can be found online at https://doi.org/10.1016/j.oregeorev.2019.01.025.

References

Biel, C., Subías, I., Acevedo, R.D., Yusta, I., Velasco, F., 2012. Mineralogical, IR-spectral and geochemical monitoring of hydrothermal alteration in a deformed and meta-morphosed Jurassic VMS deposit at Arroyo Rojo, Tierra del Fuego, Argentina. J. South Am. Earth Sci. 35, 62–73.

Chang, Y.F., Liu, X.P., Wu, C.Y., 1991. The Copper–Iron Belt of the Lower and Middle reaches of the Changjiang River. Geological Publishing House, Beijing, pp. 1–234 (in Chinese with English abstract).

Chang, Z.S., Yang, Z.M., 2012. Evaluation of inter-instrument variations among short

wavelength infrared (SWIR) devices. Econ. Geol. 107, 1479–1488.

Chen, J.F., Yan, J., Xie, Z., Xu, X., Xing, F., 2001. Nd and Sr isotopic compositions of igneous rocks from the Lower Yangtze region in eastern China: constraints on sources. Phys. Chem. Earth (A) 26, 719–731.

Duan, D.F., Jiang, S.Y., 2017. The composition of pyroxene and amphibole in ore-related pluton in Jiguanzui Au–Cu skarn deposit, Edong region: implication for the magma evolution and mineralization. Acta Petrol. Sin. 33, 3507–3517 (in Chinese with English abstract).

Duke, E.F., 1994. Near infrared spectra of muscovite, Tschermak substitution, and metamorphic reaction progress: implications for remote sensing. Geology 22, 621–624.

Guo, C.Z., Wei, Q.M., Ye, H., 2007. Occurrence of cryptoexplosive breccia and porphyry type orebodies in Jiguanzui deposit and their Characteristics. Metal Mine 368, 52–55 (in Chinese with English abstract).

Han, J.S., Chu, G.B., Chen, H.Y., Hollings, Pete, Sun, S.Q., Chen, M., 2018. Hydrothermal alteration and short wavelength infrared (SWIR) characteristics of the Tongshankou porphyry-skarn Cu-Mo deposit, Yangtze craton, Eastern China. Ore Geol. Rev. 101, 143–164.

Harraden, C.L., McNulty, B.A., Gregory, M.J., Lang, J.R., 2013. Shortwave infrared spectral analyses of hydrothermal alteration associated with the Pebble porphyry copper-gold-molybdenum deposit, Iliamna, Alaska. Econ. Geol. 108, 483–494.

Herrmann, W., Blake, M., Doyle, M., Huston, D., Kamprad, J., Merry, N., Pontual, S., 2001. Short wavelength infrared (SWIR) spectral analyses of hydrothermal alteration zones associated with base metal sulfide deposits at Rosebery and Western Tharsis, Tasmania, and Highway-Reward, Queensland. Econ. Geol. 96, 939–955.

Huang, J.H., Chen, H.Y., Han, J.S., Deng, X.H., Lu, W.J., Zhu, R.L., 2018. Alteration zonation and short wavelength infrared (SWIR) characteristics of the Honghai VMS Cu-Zn deposit, Eastern Tianshan, NW China. Ore Geology Review, pp. 263–279.

Jones, S., Herrmann, W., Gemmell, J.B., 2005. Short wavelength infrared spectral characteristics of the HW Horizon: implications for exploration in the Myra Falls volcanic-hosted massive sulfide camp, Vancouver Island, British Columbia, Canada. Econ. Geol. 100, 273–294.

Ke, Y.F., Cai, H.G., Du, K., Wu, Y.X., Yuan, H.W., 2016. Analyses of geological characteristics and prospecting potential of jiguanzui Cu-Au deposits in Daye City, Hubei Province. Resour. Environ. Eng. 30, 817–824 (in Chinese with English abstract).

Laakso, K., Rivard, B., Peter, J.M., White, H.P., Maloley, M., Harris, J., Rogge, D., 2015. Application of airborne, laboratory and field hyperspectral methods to mineral exploration in the Canadian Arctic: recognition and characterization of volcanogenic massive sulfide-associated hydrothermal alteration in the Izok Lake deposit area, Nunavut, Canada. Econ. Geol. 110, 925–941.

Laakso, K., Peter, J.M., Rivard, B., White, H.P., 2016. Short-wave infrared spectral and geochemical characteristics of hydrothermal alteration at the Archean Izok Lake Zn–Cu–Pb–Ag volcanogenic massive sulfide deposit, Nunavut, Canada: application in exploration target vectoring. Econ. Geol. 111, 1223–1239.

Li, H.Q., Chen, F.W., Mei, Y.P., 2009a. SHRIMP U-Pb zircon dating of the mineralized intrusion from Jiguanzui ore field in Eastern Hubei Province and its geological significance. Geotectonica Metallogenia 33, 411–417 (in Chinese with English abstract).

Li, X.H., Li, W.X., Wang, X.C., Qiu, L.L., Liu, L., Tang, Q.Q., Gao, Y.Y., Wu, F.Y., 2010. SIMS U-Pb zircon geochronology of porphyry Cu–Au–(Mo) deposits in the Yangtze River Metallogenic Belt, eastern China: magmatic response to early Cretaceous lithospheric extension. Lithos 119, 427–440.

Li, J.W., Zhao, X.F., Zhou, M.F., Vasconcelos, P., Ma, C.Q., Deng, X.D., Zhao, Y.X., Wu, G., 2008. Origin of the Tongshankou porphyry–skarn Cu–Mo deposit, eastern Yangtze craton, Eastern China: geochronological, geochemical, and Sr–Nd–Hf isotopic constraints. Miner. Deposita 43, 319–336.

Li, J.W., Zhao, X.F., Zhou, M.F., Ma, C.Q., Zorano Sérgio de Souza, Paulo Vasconcelos, 2009b. Late Mesozoic magmatism from the Daye region, eastern China: U-Pb ages, petrogenesis, and geodynamic implications. Contrib. Miner. Petrol. 157, 383–412.

Liu, C.M., Xu, W.S., Pang, Q.H., 1996. Geochemical exploration conceptual model of the Jiguanzui concealed copper–gold deposit, Hubei Province. Geophys. Geochem. Explor. 20, 189–197 (in Chinese with English Abstract).

Mao, J.W., Wang, Y.T., Lehmann, B., Yu, J.J., Du, A.D., Mei, Y.X., Li, Y.F., Zang, W.S., Stein, H.J., Zhou, T.F., 2006. Molybdenite Re–Os and albite $^{40}Ar/^{39}Ar$ dating of Cu–Au–Mo and magnetite porphyry systems in the Yangtze River valley and metallogenic implications. Ore Geol. Rev. 29, 307–324.

Mao, J.W., Xie, G.Q., Zhao, H.J., Wei, K.T., Jin, S.G., Pan, H.J., Ke, Y.F., 2011. Timing of skarn deposit formation of the Tonglushan ore district, southeastern Hubei Province, Middle-Lower Yangtze River Valley metallogenic belt and its implications. Ore Geol. Rev. 43, 62–77.

McLeod, R.L., Gabell, A.R., Green, A.A., Gardavsky, V., 1987. Chlorite infrared spectral data as proximity indicators of volcanogenic massive sulfide mineralization. Pacific Rim Congress'87, Gold Coast, Queensland, pp. 321–324.

Neal, L.C., Wilkinson, J.J., Mason, P.J., Chang, Z.S., 2018. Spectral characteristics of propylitic alteration minerals as a vectoring tool for porphyry copper deposits. J. Geochem. Explor. 184, 179–198.

Pan, H.J., 2004. Discussion on the simplification of the ore type of the Jiguanzui gold––copper deposit, Hubei. Gold Geology 10, 28–31 (in Chinese with English Abstract).

Pan, Y.M., Dong, P., 1999. The Lower Changjiang (Yangzi/Yangtze River) metallogenic belt, east central China: intrusion- and wall rock-hosted Cu–Fe–Au, Mo, Zn, Pb, Ag deposits. Ore Geol. Rev. 15, 177–242.

Pontual, S., Merry, N., Gamson, P., 1997. G-Mex Volume 1: Spectral interpretation field manual: Kew, Victoria 3101, Australia. Ausspec International Pty. Ltd.

Post, J.L., Noble, P.N., 1993. The near-infrared combination band frequencies of dioctahedral smectites, micas and illites. Clays Clay Miner. 41, 639–644.

Qiu, Y.J., 1995. The origin and geological characteristics of the Jiguanzi Cu (Fe)–Au deposit, eastern Hubei. Geol. Explor. Non-Ferrous Metals 4, 77–82 (in Chinese with English Abstract).

Scott, K.M., Yang, K., 1997. Spectral reflectance studies of white micas. Sydney, Australia: CSIRO Exploration and Mining Report, pp. 1–439.

Shu, Q.A., Chen, P.L., Cheng, J.R., 1992. Geology of Iron-Copper Deposits in Eastern Hubei Province, China. Metallurgic Industry Press, Beijing, pp. 1–192 (in Chinese).

Sun, Y., Seccombe, P.K., Yang, K., 2001. Application of short-wave infrared spectroscopy to define alteration zones associated with the Elura zinc–lead–silver deposit, NSW, Australia. J. Geochem. Explor. 73, 11–26.

Tappert, M.C., Rivard, B., Giles, D., Tappert, R., Mauger, A., 2013. The mineral chemistry, near-infrared, and mid-infrared reflectance spectroscopy of phengite from the Olympic Dam IOCG deposit, South Australia. Ore Geol. Rev. 53, 26–38.

Thompson, A.J., Hauff, P.L., Robitaille, A.J., 1999. Alteration mapping in exploration: application of short-wave infrared (SWIR) spectroscopy. SEG Newslett. 39, 16–27.

Wei, Q.M., Deng, G.L., Hu, Z.J., 2006. Discussion on the occurrence regularity of orebody in Jiguanzui copper-gold deposit. Gold Sci. Technol. 14, 30–33 (in Chinese).

Wei, S.K., Hu, Q.L., Jin, S.G., Wei, K.T., 2013. Genesis and deep prospecting of generalized skarn deposits in the Edong district. Resour. Environ. Eng. 27, 86–91 (in Chinese).

Xiao, B., Chen, H.Y., Hollings, Pete, Wang, Y.F., Yang, J.T., Wang, F.Y., 2018b. Element transport and enrichment during propylitic alteration in Paleozoic porphyry Cu mineralization systems: insights from chlorite chemistry. Ore Geol. Rev. 102, 437–448.

Xiao, B., Chen, H.Y., Wang, Y.F., Han, J.S., Xu, C., Yang, J.T., 2018a. Chlorite and epidote chemistry of the Yandong Cu deposit, NW China: metallogenic and exploration implications for Paleozoic porphyry Cu systems in the Eastern Tianshan. Ore Geol. Rev. 100, 168–182.

Xiao, D., Zhang, Y.Q., 2003. The formation of Au–Cu–Fe and Au–Fe ores in No.1 orebody of the Jiguanzui coproaurite deposit. Hubei Geol. Miner. Resour. 17, 18–21 (in Chinese with English abstract).

Xie, G.Q., Mao, J.W., Zhou, S.D., Ye, H.S., Yan, Q.R., Zhang, Z.S., 2006. SHRIMP zircon U-Pb dating for volcanic rocks of the Dasi Formation in southeast Hubei Province, Middle-Lower reaches of the Yangtze River and its implications. Chin. Sci. Bull. 51, 3000–3009.

Xie, G.Q., Zhao, H.J., Li, X.Q., Hou, K.J., Pan, H.J., 2009. Re–Os dating of molybdenite from Tonglushan ore district in southeastern Hubei Province, Middle-Lower Yangtze River belt and its geological significance. Miner. Deposits 28, 227–239 (in Chinese with English abstract).

Xie, G.Q., Mao, J.W., Zhao, H.J., 2011. Zircon U-Pb geochronological and Hf isotopic constraints on petrogenesis of Late Mesozoic intrusions in the southeast Hubei Province, Middle-Lower Yangtze River belt (MLYRB), East China. Lithos 125, 693–710.

Xie, G.Q., Mao, J.W., Zhao, H.J., Duan, C., Yao, L., 2012. Zircon U-Pb and phlogopite ^{40}Ar–^{39}Ar age of the Chengchao and Jinshandian skarn Fe deposits, southeast Hubei Province, Middle-Lower Yangtze River Valley metallogenic belt, China. Miner. Deposita 47, 633–652.

Xu, C., Chen, H.Y., White, Noel, Qi, J.P., Zhang, L.J., Zhang, S., Duan, G., 2017. Alteration and mineralization of Xinan Cu-Mo ore deposit in Zijinshan orefield, Fujian Province, and application of short wavelength infra-red technology (SWIR) to exploration. Miner. Deposits 36, 1013–1038 (in Chinese with English abstract).

Yang, Z.M., Hou, Z.Q., Yang, Z.S., Qu, H.C., Li, Z.Q., Liu, Y.F., 2012. Application of short wavelength infrared (SWIR) technique in exploration of poorly eroded porphyry Cu district: a case study of Niancun ore district. Tibet. Miner. Deposits 31, 699–717 (in Chinese with English abstract).

Yang, K., Lian, C., Huntington, J.F., Peng, Q., Wang, Q., 2005. Infrared spectral reflectance characterization of the hydrothermal alteration at the Tuwu Cu–Au deposit, Xinjiang. China. Miner. Deposita 40, 324–336.

Yang, K., Huntington, J.F., Gemmell, J.B., Scott, K.M., 2011. Variations in composition and abundance of white mica in the hydrothermal alteration system at Hellyer, Tasmania, as revealed by infrared reflectance spectroscopy. J. Geochem. Explor. 108, 143–156.

Zhang, G.S., 1994. Sliding structure ore-controlling model of the Jiguanzui deposit, Daye, Hubei Province. Hubei Geology 8, 34–43 (in Chinese with English abstract).

Zhang, S.T., Chen, H.Y., Zhang, X.B., Zhang, W.F., Xu, C., Han, J.S., Chen, M., 2017a. Application of short wavelength infrared (SWIR) technique to exploration of skarn deposit: a case study of Tonglvshan Cu-Fe-Au deposit, Edongnan (southeast Hubei) ore concentration area. Miner. Deposits 36, 1263–1288 (in Chinese with English abstract).

Zhang, S.T., Chen, H.Y., 2018. Magmatic evolution, alteration mineral characteristics and application to exploration in the Tonglvshan Cu–Fe–Au deposit, Hubei Province, China. Guangzhou Institute of Geochemistry, Chinese Academy of Sciences Press, Guangzhou, pp. 1–198 (in Chinese).

Zhang, G.S., Jin, S.G., Hu, Q.L., Huang, Z.H., Yuan, H.W., 2011. Structural characteristics and ore-controlling effect of Jiguanzui deposit. Resour. Environ. Eng. 25, 11–14 (in Chinese with English abstract).

Zhang, W., Li, J.W., 2015. Ore Genesis of the Jiguanzui Cu–Au Deposit in Southeastern Hubei Province, China. China University of Geosciences Press, Wuhan, pp. 1–127 (in Chinese).

Zhang, Y., Shao, Y.J., Li, H.B., Liu, Z.F., 2017c. Genesis of the Xinqiao Cu–S–Fe–Au deposit in the Middle-Lower Yangtze River Valley metallogenic belt, Eastern China: constraints from U-Pb-Hf, Rb-Sr, S, and Pb isotopes. Ore Geol. Rev. 86, 100–116.

Zhang, Y., Shao, Y.J., Chen, H.Y., Liu, Z.F., Li, D.F., 2017b. A hydrothermal origin for the large Xinqiao Cu-S-Fe deposit, Eastern China: evidence from sulfide geochemistry and sulfur isotopes. Ore Geol. Rev. 88, 534–549.

Zhang, Y., Shao, Y.J., Zhang, R.Q., Li, D.F., Liu, Z.F., Chen, H.Y., 2018. Dating ore deposit using garnet U-Pb geochronology: example from the Xinqiao Cu–S–Fe–Au deposit. Eastern China. Miner. 8, 31.

Zhang, W., Wang, H.D., Deng, X.D., Hu, H., Li, J.W., 2016. Mineralogy of the Au–Ag–Bi–Te–Se assemblages in the Jiguanzui Cu–Au skarn deposit, Daye District,

southeastern Hubei Province. Acta Petrol. Sin. 32, 456–470 (in Chinese with English abstract).

Zhang, J.B., Zhu, Z.X., 2005. The understanding of magma rock and mineralization rule in Jiguanzui copper–gold deposit. Gold Sci. Technol. 13, 2–5 (in Chinese with English abstract).

Zhao, Y.M., Zhang, Y.N., Bi, C.S., 1999. Geology of gold-bearing skarn deposits in the middle and lower Yangtze River Valley and adjacent regions. Ore Geol. Rev. 14, 227–249.

Zhou, T.F., Fan, Y., Yuan, F., Zhong, G.X., 2012. Progress of geological study in the Middle-Lower Yangtze River Valley Metallogenic belt. Acta Petrol. Sin. 28, 3051–3066.